HHS Public Access

Author manuscript

Comput Fluids. Author manuscript; available in PMC 2018 January 17.

Published in final edited form as:

Comput Fluids. 2017 January 17; 143: 16–31. doi:10.1016/j.compfluid.2016.10.032.

Multiblock High Order Large Eddy Simulation of Powered Fontan Hemodynamics: Towards Computational Surgery

Yann T. Delorme[a,*], **Mark D. Rodefeld**[b], and **Steven H. Frankel**[a]

[a]Faculty of Mechanical Engineering, Technion-Israel Institute of Technology, Haifa, Israel

[b]Department of Surgery, Indiana University School of Medicine, Indianapolis, USA

Abstract

Children born with only one functional ventricle must typically undergo a series of three surgeries to obtain the so-called Fontan circulation in which the blood coming from the body passively flows from the Vena Cavae (VCs) to the Pulmonary Arteries (PAs) through the Total Cavopulmonary Connection (TCPC). The circulation is inherently inefficient due to the lack of a subpulmonary ventricle. Survivors face the risk of circulatory sequelae and eventual failure for the duration of their lives. Current efforts are focused on improving the outcomes of Fontan palliation, either passively by optimizing the TCPC, or actively by using mechanical support. We are working on a chronic implant that would be placed at the junction of the TCPC, and would provide the necessary pressure augmentation to re-establish a circulation that recapitulates a normal two-ventricle circulation. This implant is based on the Von Karman viscous pump and consists of a vaned impeller that rotates inside the TCPC. To evaluate the performance of such a device, and to study the flow features induced by the presence of the pump, Computational Fluid Dynamics (CFD) is used.

CFD has become an important tool to understand hemodynamics owing to the possibility of simulating quickly a large number of designs and flow conditions without any harm for patients. The transitional and unsteady nature of the flow can make accurate simulations challenging. We developed and in-house high order Large Eddy Simulation (LES) solver coupled to a recent Immersed Boundary Method (IBM) to handle complex geometries. Multiblock capability is added to the solver to allow for efficient simulations of complex patient specific geometries. Blood simulations are performed in a complex patient specific TCPC geometry. In this study, simulations without mechanical assist are performed, as well as after virtual implantation of the temporary and chronic implants being developed. Instantaneous flow structures, hepatic factor distribution, and statistical data are presented for all three cases.

*Corresponding author: delorme.yann@gmail.com (Yann T. Delorme).

Keywords

Powered Fontan Hemodynamics; Large Eddy Simulation; Computational Surgery; Multiblock Immersed Boundary Method

1. Introduction

Single ventricle heart disease is the leading cause of death from any birth defect in the first year of life ([8, 21]). The most common of these defects is hypoplastic left heart syndrome, in which the only functional ventricle is a morphologically right ventricle [15]. The current procedure to overcome this uni-ventricular condition is to by pass the right sided circulation and rely upon the single functional ventricle to supply the systemic and pulmonary circulations in series. This reparative process is known as staged Fontan palliation. The Fontan circulation is an inherently inefficient circulation due to the lack of a sub-pulmonary ventricle, and is associated with elevated systemic venous pressures and reduced ventricular filling [12]. Even though the existing staged palliative approach results in significant improvement in survival, it remains highly problematic with only 50 to 70% survival rate through completion of all three surgeries ([39, 6]). In addition there is a persistent risk of late Fontan failure which stems form the residual circulatory inefficiencies after completion of palliation [43]. These complications may be attributed to energy losses and irregular flow and mixing features in the TCPC.

Passive flow solutions focus on improving the configuration of the TCPC to reduce pressure losses and improve flow split between the two lungs. To prevent the two inflow jets from colliding, groups have proposed a model of TCPC with planar one-diameter offset between the superior and inferior vena cavae. This solution proved to reduce power losses by preventing inflow collision [33]. Another strategy is to split one or both vena cavae to prevent the flow from colliding, while maintaining a good flow split in order for the hepatic factor to be equally distributed between the two lungs [51, 30]. However, these modifications may be difficult to implement surgically with concern for thrombus formation and injury to adjacent anatomic structures: the pressure benefit is relatively small with respect to clinical improvement. Thus a clinical benefit of passive flow optimization has yet to be proven. Active flow control solutions focus on augmenting Fontan flow through the use of a mechanical device. The aim is to resolve the Fontan paradox (increase in the systemic venous pressure and a decrease in the pulmonary arterial pressure) by decreasing systemic venous pressure and increasing pulmonary arterial pressure ([10, 12, 42]) as occurs in normal circulatory physiology. We have shown that a pressure increase of as little as 2 to 5 mmHg will reduce systemic venous pressure and increase pulmonary arterial pressure, and restore conditions closer to a normal two ventricle circulation [44]. Mechanical assist consisting of a single axial pump positioned in the inferior vena cava has been proposed [55], increasing the pressure before reaching the junction of the TCPC. But this represents a partial solution to the 4-way flow problem. We have proposed a pump solution based on the Von Karman viscous pump principle which involves spinning a double-sided cone at the center of the TCPC junction, featuring mild vane structure [45]. This solution addresses all 4 flow components of the TCPC with a single pump.

Placing a right sided power source in the uni-ventricular Fontan circulation would restore conditions closer to a normal two-ventricle circulation as potential to eradicate the conditions which lead to Fontan failure and allow medical management of affected patients as a “bi-ventricular Fontan”. Two versions of this pump are currently under development: a temporary implant and a chronic implant. In the case of the temporary implant, the VIP would be inserted via a catheter through a femoral vein or jugular vein, positioned at the TCPC junction and deployed by an expandable pump head configuration. The VIP will be powered by an external electromagnetic motor. Kerlo *et al* [25] show the hydraulic performances of the VIP over a range of flow rates and rotation rates. The VIP provides the desired pressure rise for the selected rotation rates, with a relatively flat profile over the range of flow rates. This predicts stable performance over a wide range of physiological conditions. The operating conditions for the pump are between 2000 RPM and 5000 RPM (up to 7000 RPM if needed).

In the case of the chronic implant, an impeller with contained motor is located at the center of a housing which has been optimized to improve pump performance. This device would be implanted permanently and would replace the existing TCPC junction. Figure 1 shows a schematic of the implantation of the chronic implant: starting from an existing TCPC configuration (Figure 1-a), the junction of the TCPC would be removed (Figure 1-b) and the vessels would be directly sutured into the inlets and outlets of the device (Figure 1-c). Figure 2 shows an early stage prototype. For flow visualization purposes, the housing is transparent and the VIP can be seen at the center of the junction. The VIP is maintained in place by the two shafts, and the electric motor is located inside the pump itself. Thanks to the presence of its housing, the chronic implant is independent from the existing blood vessel configuration: the device can be implanted in patients for which the implantation of the temporary implant would have been problematic due to the geometry of the TCPC junction.

Computational Fluid Dynamics (CFD) is widely used to study pathological flows and medical devices. In 2001, Mittal *et al* [35] used Large Eddy Simulation (LES) to study pulsatile flow in a modeled arterial stenosis. They showed good qualitative agreement with experiments, with an accurate prediction of the transitional flow behind the stenosis, even with a laminar inflow condition. They emphasized the ability of LES to predict transitional and turbulent flows, as opposed to RANS based approaches. Similarly, Bazilevs *et al* proposed a variational multiscale residual-based turbulence model for LES [7] and showed accuracy of flow predictions for bilogical applications. In 2007, Varghese *et al* [56, 57] used DNS to study axi-symmetric flows under steady and pulsatile conditions. Under steady inflow conditions, they showed that the flow was laminar in the entire domain for an inlet Reynolds number Re = 500. But at Re = 1000, they showed that the flow transitioned to a turbulent flow, with a delayed transition downstream of the stenosis. This effect was even larger for the eccentric case. These studies showed the importance of a good turbulence model to capture the transitional and turbulent nature of blood flows due to the shape and curvatures of the vessels. CFD is also commonly used to study medical devices (axial and centrifugal pumps, mechanical heart valves…) [4, 53, 58, 52].

For years, people have been trying to better understand the flow physics induced by the TCPC geometries to reduce the pressure losses and improve the outcome of the Fontan

procedure. Early studies investigated the impact of geometric parameters such as curvature, diameter or offset on the efficiency of the geometry. Most studies were performed on idealized geometries with rigid walls. Recently, studies showed that patient specific geometries [46] with physiological boundary conditions [34] are necessary to obtain accurate flow predictions. Also recent studies emphasized the need for high order accurate numerical methods to predict small scale vortical structures responsible for part of the energy losses [26].

With the improvement of computational power, the concept of computational surgery has become more and more popular over the past several years. The idea is to use CAD and CFD software to simulate the effects of different blood vessel configurations, or different implantation of medical device before performing the actual surgery [29, 13, 1, 31, 32]. In this paper, the performance of our novel temporary and chronic implants are studied using a novel multiblock Large Eddy Simulation solver coupled with an Immersed Boundary Method. The simulations are performed in a patient specific geometry. The temporary implant is placed at the junction of the TCPC, while a computational surgery is performed to implant the chronic device with the guidance of surgeons. Instantaneous flow features, as well as pressure rise, mean wall shear stresses and hemolysis index are studied to characterize the powered Fontan hemodynamics in a patient specific geometry.

2. Methods

2.1. Governing Equations

To study the flow physics induced by the Fontan circulation, a high order Large Eddy Simulation code has been developed based on a dimensionless incompressible formulation of the Navier-Stokes equations, as presented below:

$$\frac{\partial \tilde{u}_i}{\partial t}+\tilde{u}_j\frac{\partial \tilde{u}_i}{\partial x_j}=-\frac{\partial \tilde{p}}{\partial x_i}+\frac{1}{Re}\frac{\partial^2 \tilde{u}_i}{\partial x_j \partial x_j}-\frac{\partial \tau_{ij}}{\partial x_j} \quad (1)$$

$$\frac{\partial \tilde{u}_i}{\partial x_i}=0 \quad (2)$$

where $\tilde{u}_i$ is the i^{th} component of the spatially filtered velocity vector, $\tilde{p}$ is the spatially filtered pressure, x_i is the i^{th} component of the spatial domain and τ_{ij} is the sub-grid stress tensor which arises from the filtering of the equations. In Large Eddy Simulation, the flow scales are separated through filtering operations, from which arise the sub-grid scale tensor τ_{ij}. The classical eddy viscosity model yields [41]:

$$\tau_{ij}=-2\nu_T S_{ij} \quad (3)$$

with

$$S_{ij}=\frac{1}{2}\left(\frac{\partial\tilde{u}_i}{\partial x_j}+\frac{\partial\tilde{u}_j}{\partial x_i}\right). \quad (4)$$

The eddy viscosity ν_T is specified in terms of gradients of the filtered velocity field according to the Vreman model [49]. This model is easy to implement, efficient to use, and applicable to fully inhomogeneous turbulent flows[3, 13, 14, 49]. This model gives:

$$\nu_T=C\Pi^g \quad (5)$$

$$\Pi^g=\sqrt{\frac{B_\beta}{\alpha_{ij}\alpha_{ij}}} \quad (6)$$

with

$$\alpha_{ij}=\frac{\partial\tilde{u}_j}{\partial x_i} \quad (7)$$

and

$$\begin{cases} \beta_{ij} & =\sum_{m=1}^{3}\Delta_m^2\alpha_{mi}\alpha_{mj} \\ B_\beta & =\beta_{11}\beta_{22}-\beta_{12}^2+\beta_{11}\beta_{33}-\beta_{13}^2+\beta_{22}\beta_{33}-\beta_{23}^2 \end{cases}. \quad (8)$$

A value of 0.07 was proposed by Vreman for the constant C and has been used in this study.

2.2. Numerical Methods

The equations are integrated in time using a third order accurate Backward Difference Formula (BDF) method [50]. The convective terms are integrated using a fifth order accurate Weighted Essentially Non Oscillatory (WENO) scheme [59]. The diffusion terms and the sub-grid stress tensor arising from the filtering of the equations are computed using fourth order accurate centered difference schemes. The implementation of the methods were tested and validated in our previous studies[3, 13, 14].

2.3. Multiblock Immersed Boundary Method and Computational Surgery

2.3.1. Immersed Boundary Method—The use of high order numerical methods is simplified by the use of a Cartesian grid. But to efficiently simulate flows over or through non-Cartesian geometries a mirroring immersed boundary method (IBM) is used [28]. Using

this approach, it is possible to simulate complex geometries such as complex blood vessel configurations on a simple Cartesian grid.

2.3.2. Multiblock Approach Towards Computational Surgery—Multi-block approaches have been more and more popular, especially since the increase in available computational resources. Applications of multi-block CFD are also very wide [38, 11, 37, 36, 54, 16, 47, 27].

In our approach the multi-domain decomposition is performed using message passing interface (MPI). Each processor is assigned particular section of the computational domain. To ensure continuity of the solution across the processors, overlapping is used, as seen on figure 3. Figure 3-a shows a computational domain partitioned using four processors (red, black, blue and green). Each processor only solve the Navier-Stokes equations on their particular domain. Figure 3-b shows the overlapping between each processor. In this example, two layers of grid points are shared between the processors: at each time step, before computing the spatial derivatives, the processors communicate the shared data to their neighbors. By doing so, we make sure the the values of these derivatives are going to be identical at the interface between the processors. The needed number of shared grid points depends on the numerical schemes the solver uses. In our case, three layers of grid points were used.

2.3.3. Poisson Solver—The Poisson equation now has to be solved in parallel, each processor solving the problem on their part of the computational domain. To do so, the *Hypre* library is used ([17],[18],[19]). A preconditioned conjugate gradient (PCG) method is used with geometric multigrid as preconditioner for solving the discretized Poisson equation as described in Ashby *et al* [5].

2.3.4. Automation of the Process—When using a limited number of processors, the decomposition of the domain can be performed manually. But this task becomes very tedious when considering a large number of processors. Indeed, for each processor, the sub-domain has to be defined, as well as the connectivity between each block (each block has to know the identity of its neighbors to know with which processor to communicate). To easily setup a complex geometry with large number of blocks, a pre-processing code was written. This code iterates to find the optimal configuration of the blocks to limit the number of grid points wasted. The algorithm is summarized in figure 4. The user inputs the number of minimum number of processors desired for the simulation, as well as a surface mesh of the geometry of interest. The code then computes the dimensions of the global bounding box necessary to fit the geometry, as well as the levelset function φ inside this box (positive values inside the fluid region, negative values inside the solid region). To keep the load between processors as balanced as possible, it is theorized that the number of processors in each direction should be proportional to the size of the domain in each direction. Starting with N = 1 for the smaller size direction, the number of processors in the other directions is computed using the ratio of the length of the bounding box. Once the number of blocks in each direction is known, each block containing at least one grid point for which ϕ is greater or equal to 0 is flagged. After this operation, the number of flagged block is computed and if this number is less than the desired number, the number of blocks in the smallest direction is

increased. The process is repeated until the number of flagged blocks is equal or greater than the desired number of blocks. The code then generates the connectivity between the processors, to allow for the communication during the LES simulation.

2.3.5. Scaling and Efficiency of the Solver—Figure 5-a shows the scaling of the multi-block solver. As the number of grid points increases (black and blue), the code scales linearly up to 512 processors.

To assess the efficiency (ratio between the number of fluid grid points and the total number of grid points) of the multiblock decomposition, two geometries are considered. The first one is an idealized TCPC used to study powered Fontan hemodynamics in [13] (figure 6-a). The second one was obtained from the Open Source Medical Software Corporation [40] and corresponds to a three year old male patient (figure 6-b). Figure 5-b shows the efficiency for these two cases. For the idealized TCPC, the geometry is very simple and symmetric, which makes the improvement of the computational efficiency easier. On a single block domain, and in the absence of grid stretching, the efficiency is close to 20%. Very quickly, as the number of blocks increases, the efficiency increases and with less than 40 blocks, it reaches 70%. For the patient specific geometry, it is more difficult to obtain a high grid efficiency due to the high number of small vessels. With the single block approach, the grid efficiency is close to 8%. As the number of blocks increases, the efficiency increases too, and is close to 40% for about 1400 blocks.

The same comments can be made when looking at the the ratio of the computational domain volume for the multi-block approach with the volume of the computational domain for the single block approach. When the number of blocks is low, the behavior of the multi-block approach is similar for both geometries. As the number of blocks increases, a plateau is reached for the idealized TCPC around 700 blocks. This shows that the blocks are following closely the geometry, and that more blocks are not going to improve the efficiency of the solver. For the patient specific geometry, a similar plateau is observed after around 1300 blocks.

2.3.6. Overall procedure—In the rest of this study, the following procedure for the setup of a simulation is applied. The blood vessels configurations are obtained from MRI data [40] and are imported into a CAD software (here *DS Solidworks*), as shown on figure 7-a. If needed the geometry is modified and then exported to be then used by a meshing software (in this case *Gambit*). A surface mesh of the geometry is then generated (Figure 7-b). This surface is then used by the pre-processing software to generate an optimal configuration of the computational domain based on the desired number of blocks (Figure 7-c). This overall procedure is very fast as it does not involve a complex mesh generation.

2.4. Particle Laden Flows for Hemolysis Estimation

Particle modeling has become more and more popular in the past decade. In 2008, Guha [22] reviewed most of the current methods used to model particle transport and particle deposition. Most of the models assumed a dilute mixture, in which the volume fraction of the dispersed phase is low. With this assumption, the particles are not interacting with each other and they exhibit a one way coupling (the motion of the particles depends on the fluid

flow field). Most of the previously cited papers assumed that the density ratio between the particles and the surrounding fluid is large enough ($O(100)$) to neglect any other forces that could drive their movements. In the case of blood flow, the density ration is much closer to unity. Because of this, four forces need to be taken into account: the aerodynamic drag, the gravity, the pressure drag and the Basset force drag [2]. The aerodynamic drag ca be written as

$$F_D = \frac{V_f - V_p}{\tau_r} \quad (9)$$

where V_f is the velocity of the fluid at the article location, V_p is the velocity of the particle and τ_r is the particle relaxation time. It is a measure of inertia and denotes the time scale with which any slip velocity between the particle and the fluid is equilibrated. In the case of a spherical particle, we have:

$$\tau_r = \frac{2\rho_p r^2}{8\mu} \quad (10)$$

where ρ_p is the density of the particle, r is the radius of the particle and μ is the viscosity of the fluid. Another much used equation is shown here:

$$C_D = \frac{24}{Re_p}\left(1 + 0.15 Re_p^{0.687}\right). \quad (11)$$

It relates the drag coefficient on the particle as a function of the Reynolds number relative to the particle. If the particles are non-spherical, the aerodynamic drag is usually expressed as an empirical correlation to the drag of equivalent spheres by introducing suitable shape factors. The gravitational forces are a function of the relative difference between the density of the particle and the density of the fluid flow. It can be expressed as:

$$F_{Gi} = \left(1 - \frac{\rho_f}{\rho_p}\right) g_i. \quad (12)$$

The pressure drag is due to the pressure gradient of the undisturbed flow, as well as the viscous stresses. It can be expressed as:

$$F_{Pi} = \frac{Du_i}{Dt} = -\frac{\partial p}{\partial x_i} + \frac{1}{Re}\frac{\partial^2 u_i}{\partial x_j \partial x_j}. \quad (13)$$

The Basset drag force describes the force due to the lagging boundary layer development with changing relative velocity of bodies moving through a fluid. The Basset term accounts

for viscous effects and addresses the temporal delay in boundary layer development as the relative velocity changes in time. It can be expressed as:

$$F_{Bi}=\frac{\rho_f}{\rho_p}\frac{9}{\sqrt{\pi}d_p\sqrt{Re}}\int_0^t\frac{1}{\sqrt{t-\tau}}\frac{d}{d\tau}(u_i-V_{pi})\,d\tau \quad (14)$$

where d_p is the dimensionless diameter of the particle and t is the current time. The equations of motion is then:

$$\frac{dV_{pi}}{dt}=F_{Di}+F_{Gi}+F_{Pi}+F_{Bi} \quad (15)$$

and

$$\frac{dx_i}{dt}=V_{pi}. \quad (16)$$

2.4.1. Time Integration—Following the approach of Armenio *et al* [2], in dimensionless form:

$$Re_p=Re\times D_p\times\left((V_f-V_p)^2\right)^{1/2} \quad (17)$$

and

$$F_D=\frac{18}{\left(\frac{\rho_p}{\rho_f}\right)\times Re\times D_p^2}\left(1+0.15Re_p^{0.667}\right)\times(V_f-V_p). \quad (18)$$

The pressure drag is computing by interpolating the pressure gradients and viscous terms from the Eulerian computational grid to the Lagrangian location of each particle. The computation of the Basset drag force is more complicated. Indeed, using a regular quadrature rule to compute the time integral is not possible as the integral is not defined at $\tau = t$. Applying a single quadrature rule:

$$\int_0^t\frac{1}{\sqrt{t-\tau}}f(\tau)d\tau=\sum_{k=1}^{N}\left(\int_{(k-1)\Delta t}^{k\Delta t}\frac{1}{\sqrt{t-\tau}}f(\tau)d\tau\right) \quad (19)$$

where N is the number of time interval used to compute the integral. Assuming that the function f is relatively constant of the interval $[(k-1)\,\Delta t; k\Delta t]$, we can write:

$$\sum_{k=1}^{N}\left(\int_{(k-1)\Delta t}^{k\Delta t}\frac{1}{\sqrt{t-\tau}}f(\tau)d\tau\right)=\sum_{k=1}^{N}\left(\frac{1}{2}(f\left((k-1)\Delta t\right)+f\left(k\Delta t\right))\int_{(k-1)\Delta t}^{k\Delta t}\frac{1}{\sqrt{t-\tau}}d\tau\right). \quad (20)$$

We finally obtain:

$$\int_0^t\frac{1}{\sqrt{t-\tau}}f(\tau)d\tau=\sum_{k=1}^{N}\left(\frac{1}{2}(f\left((k-1)\Delta t\right)+f\left(k\Delta t\right))\left(\sqrt{t-(k-1)\Delta t}-\sqrt{t-k\Delta t}\right)\right). \quad (21)$$

Equations 15 and 16 are then integrated using a first order accurate Euler scheme with multiple sub-steps. This is done to make sure that the particle does not cross too many cells between two consecutive time steps.

2.4.2. Bouncing Boundary Condition at the Surface of the Immersed Body—In a case of collision of a particle with the immersed body, a perfectly elastic collision is assumed with the tangential component of the velocity before and after the collision constant and the normal component of the velocity that changes sign between before and after the contact.

2.4.3. Hemolysis Estimation—Damage to the red blood cell with resulting release of hemoglobin into the blood plasma is known as hemolysis. The trauma endured by a red blood cell can manifest several ways: morphological changes, shortened life span or even rupture. When the latter occurs, the red blood cells release hemoglobin into the blood stream. Hemolysis is mostly linked to the exposure of red blood cells to shear stresses, but also to the exposure time to these high stresses. When using Lagrangian particle tracking to estimate hemolysis, the stress history is integrated along a flow path line. These path lines can be artificially defined as a post processing once the simulation is over. But they can also but modeled using particles that follow flow pathlines between the inlet(s) and the outlet(s). All models assume that, even though the shear stress varies throughout a medical device, over a short enough time the shear stress can be considered uniform and therefore hemolysis for this time interval can be calculated using equation 22:

$$HI(\%)=\frac{\Delta H_b}{H_b}\times 100=Ct^{\alpha}\tau^{\beta}. \quad (22)$$

where C, α and β are obtained empirically to match experimental measurements. t is the exposure time and τ is a measure of the stress applied to the red blood cell. The hemolysis for each interval can then be integrated along each path line and the average of each hemolysis index at the outlet(s) can be computed. A common model to compute this integral is shown below [48, 23]:

$$HI = \int_{inlet}^{outlet} C \times \tau^{\beta} \times dt_{exposure}^{\alpha} = \sum_{inlet}^{outlet} 1.8 \times 10^{-6} \times \tau^{1.991} \times \Delta T^{0.765} \quad (23)$$

In equations 22 and 23, $\boldsymbol{\tau}$ represents a measure of the shear stress experienced at a particular time by a red blood cell. The generally accepted expression for $\boldsymbol{\tau}$ is an expression based on the Von Mises criteria, as shown below:

$$\tau = \left(\frac{1}{6} \sum (\sigma_{ii} - \sigma_{jj}) (\sigma_{ii} - \sigma_{jj}) + \sum \sigma_{ij} \sigma_{ij} \right)^{1/2}. \quad (24)$$

The definition of $\boldsymbol{\sigma_{ij}}$ is where research groups do not necessarily agree. In most recent studies, research groups used RANS-based solver to study medical devices, and they argued the need to take both shear stresses and Reynolds stresses to take into account turbulent fluctuations of the velocity field as an extra source of stress for the red blood cells [9]. In this case, we obtain:

$$\sigma_{ij} = \mu \left(\frac{\partial \overline{u}_i}{\partial x_j} + \frac{\partial \overline{u}_j}{\partial x_i} \right) - \rho \overline{u_i' u_j'}. \quad (25)$$

The idea here is that the mean flow field is not enough to estimate the stresses that red blood cells experience. Therefore, turbulence statistics should be taken into account when estimating the hemolysis index. In a recent paper, Ge *et al* [20] argued that Reynolds stresses should not be taken into account when computing blood damage. Indeed, viscous stresses are a real measure of the strength of the forces exerted by the flow on the blood cells. But Reynolds stresses are a statistical quantity that has no direct link to any physical forces. Taking into account Reynolds stresses poses another problem: the magnitude of Reynolds stresses are usually several order of magnitude higher than the magnitude of viscous stresses. In the present study, only the viscous forces were taken into account to estimate the hemolysis induced by the presence of the rotating device.

3. Results

3.1. Validation

To validate the implementation of the multiblock solver, the powered Fontan hemodynamics case at 2000 RPM from Delorme *et al.* [13] in an idealized TCPC is used. This case was previously simulated using a single block version of the solver, resulting in poor agreement when compared to SPIV measurements. The idealized TCPC consists in two inlet pipes of 22 mm corresponding to the SVC and IVC and two outlet pipes of 18 mm corresponding to the LPA and RPA. At each inlet, a flow rate of 2.2 $L.min^{-1}$ is imposed, the density is 1060 $kg.m^{-3}$ and the viscosity is 3.5 cP. This results in a Reynolds number of 700. In the present study, the simulation was performed on a domain composed of 57 blocks as seen on Figure 6-a, using a 60×60×60 grid within each block resulting in about 12.3 million grid points.

The statistics were averaged over 20 flow through times and the results are shown on figure 8.

The results in red show clearly better agreement when compared to the experimental measurements. Near the location of the rotating impeller, the re-circulation of the flow is well captured by the solver (Figure 8-a), as well as the rate at which the flow re-develops towards a typical turbulent channel flow profile as we move downstream in the PA. Similar comments can be made when looking at figures 8-b and c. The multiblock configuration allowed us to simulate this problem using more grid points, and more efficiently as most of these grid points were located inside the fluid region of interest.

3.2. Cases

3.2.1. Computational Surgery—The validated solver is now used to study the effect of the prototype on the physiology of an existing patient. The patient specific geometry was obtained from the Open Source Medical Software Corporation's website [40] and corresponds to a 17 year old female patient as seen on figure 9-a. The geometry contains 2 inlets (IVC and SVC) and 26 outlets corresponding to the different pulmonary branches. This geometry was chosen because of the adult size of the vessels, matching the size of the currently designed prototype. Using the help of surgeons, the computational surgery was performed as seen on figure 9. First, the location of the geometry that needs to be removed was chosen (Figure 9-b), and the junction of the TCPC was separated from the other vessels (Figure 9-c). The chronic implant was then put in place (Figure 9-d). Because the diameters of the blood vessels were not exactly matching the inlet and outlet diameters of the device, the ends of the blood vessels were slightly modified using CAD software. Finally the vessels were sutured on the chronic implant as seen on figure 9-e.

Figure 10 shows a summary of the three cases that are studied here. First, the original patient specific configuration (Figures 10-a and b) will be studied to estimate the energy losses due to the Fontan circulation and will serve as a baseline case to estimate the improvements due to the presence of the rotating impeller. Then the temporary implant configuration will be studied (Figures 10-c and d): in this configuration, the VIP is placed at the junction of the existing TCPC. In this particular case, the VIP was placed and centered as much as possible to maximize its distance with the blood vessels, thus reducing as much as possible the resulting wall shear stresses. Finally the chronic implant configuration (Figures 10-e and f) will be studied to estimate the improvement due to the presence of the housing replacing the original TCPC junction.

3.2.2. Multiblock Configuration—All the simulations were run with a multiblock configurations as shown on Figure 11. Figure 11-a shows the setup for the un-powered case, as well as the temporary implant case. The simulations were run with 197 blocks, each blocks containing $50 \times 50 \times 50$ grid points, resulting in 24.625 million points. Figure 11-b shows the setup for the chronic implant case. The simulations were run on 177 blocks, each blocks containing a $50 \times 50 \times 50$ grid resulting in 22.125 million grid points. The grid resolution was chosen based on a convergence study performed for the un-powered case on

three different grids (40^3, 50^3 and 60^3 points per block): convergence was achieved for the time averaged data for the 50^3 grid.

3.2.3. Boundary conditions—At each inlet, the velocity profile was imposed as a Dirichlet boundary condition. Flow information were obtained from MRI data [40]. At the SVC, a time average flow rate of 1.11622 L $\cdot$ min^{-1} was imposed, while a time averaged flow rate of 1.82512 L $\cdot$ min^{-1} was imposed at the IVC, resulting in a 32% / 68% flow split. The resulting velocity profiles at each inlet are shown on figure 12. Four time points along the signal are highlighted: these points correspond to the peak velocity (t_1), the maximum deceleration point (t_2), the minimum velocity (t_3) and the maximum acceleration point (t_4). These points are going to be used in Section 3.4 to describe the hemodynamics induced by the different configurations. To compute the averaged quantities such as the mean wall shear stress, the data were averaged over 25 cardiac cycles. At the outlets, a homogeneous Neumann boundary condition is imposed for all three velocity components.

At each inlet a homogeneous Neumann boundary condition was imposed for the pressure. At each outlet, a constant Dirichlet pressure boundary condition was imposed. Clinical data [40] show that the pressure at each PA is 17 mmHg. Thus an equal constant pressure was imposed at all the pulmonary outlets. Clinical data show a pressure drop of about 1 mmHg between inlets and outlets. These data will be used to validate the energy losses predicted by the multiblock solver in Section 3.3.

3.3. Pump Efficiency

Figure 13 shows the time averaged pressure rise between the vena cavae and the pulmonary arteries. It is defined as:

$$\Delta p = \left(\frac{1}{N_{outlets}} \sum_{outlets} p_o \right) - \left(\frac{1}{N_{inlets}} \sum_{inlets} p_i \right) \quad (26)$$

We observe pressure drops of 1.5 mmHg across the TCPC due to energy losses in the TCPC junction, which is consistent with available clinical data [40].

In the presence of the temporary implant rotating at 3000RPM, a pressure rise of about 1.7 mmHg can be observed. This pressure rise is lower than the pressure rise measured in an idealized TCPC at the same rotation rate (about 3mmHg) [13]. This indicates a sensitivity of the performance of the pump on the configuration of the blood vessels, that further motivates the use of a housing around the impeller to limit the effect of the vessel configuration on the performance of the device. The presence of the housing clearly improves the performance of the VIP, as seen on Figure 13. At 1000RPM, the pressure rise is close to 0.75 mmHg, but at 3000 RPM we reach a value of 2.6 mmHg. This latest value is close to the value in the idealized TCPC configuration, showing that it is possible to improve the performance of the impeller thanks to the housing, no matter what the initial blood vessel configuration is.

3.4. Instantaneous Flow Structures

The hemodynamics induced by the configuration of the vessels, with and without mechanical support is complex. To characterize the flow, instantaneous snapshots at the four time points highlighted in Section 3.2.3 will be shown. At every time point, isosurfaces of λ_2 colored by vorticity magnitude will be shown, as well as three dimensional streamtraces colored by velocity magnitude. The λ_2 criterion allows the identification of vortices in a complex 3D flow [24], while the streamtraces allow for a better visualization of the instantaneous motion of the flow. Figures 14 and 15 show instantaneous flow features in the case of no mechanical support. Figures 14-a and b show complex vortical structures at the peak of the inflow velocity with three main vortex tubes, resulting in helical flows at the TCPC junction, as well as in the pulmonary arteries. This complex turbulent flow, induced by the collision of the two incoming jets, results in energy dissipation that explains the drop of pressure across the TCPC. As the inflow is slowing down (Figures 14-c and d), the fluid inside the domain has more freedom to move inside the blood vessels, resulting in a breakdown of the vortex tubes into smaller vortical structures, generating more re-circulation inside the TCPC junction. It can also be observed that some re-circulation due to the curvature of the SVC is happening. As the flow reaches its minimum velocity (Figures 15-a and b), the turbulence level drops drastically resulting in less vortical structures, and low speed re-circulating flow. Many re-circulation regions are now seen inside the SVC as well as the TCPC junction and pulmonary arteries. This regions corresponds to regions where the curvature of the vessels is large. When the flow is re-accelerating (Figures 15-c and d), this re-circulating structures are being convected downstream inside the pulmonary arteries, and are being replaced by long vortex tubes, resulting in helical flow at the junction of the TCPC.

Figures 16 and 17 show instantaneous flow features for the temporary implant case at the same four time points. Figures 16-a and b show the instantaneous vortical structures at the peak velocity. Compared to the no support case, it can be seen that the flow in the TCPC junction is more complex due to the presence of the rotating impeller. Finer vortical structures can be observed, and are being shed by the tips of the six vanes of the impeller. This flow structures are then being convected by the mean flow inside the pulmonary arteries. When looking at the streamtraces, some pre-rotation of the flow can be observed near the pump in the VCs. In the PAs, a helical flow can be seen. As the flow is decelerating (Figures 16-c and d), this time the flow is not as free to develop due to the rotation of the pump that is maintained constant. The pump keeps shedding complex vortical structures, but this time this structures are not convected as fast as earlier, and have more time to dissipate before leaving the computational domain. Near the pump, because of the lower ”axial” velocity component, the flow becomes highly rotating and helical. The flow upstream from the pump stays similar, and is drive more by the motion of the VIP than the inflow condition. As the flow keeps decelerating to reach its minimum velocity (Figures 15-a and b), the flow structures generated by the VIP are almost static and do not propagates downstream of the pump. This results in a highly chaotic flow near the pump, that is now totally driving the dynamic of the flow. Similarly to the un-powered case, re-circulating regions can be seen in some of the high curvature parts of the VCs. Finally, as the flow re-accelerates (Figures 17-c and d), the vortical structures shed by the vanes of the impeller and being once again pushed

inside the pulmonary arteries, resulting in less re-circulation and chaos in the vicinity of the VIP. A more regular helical flow can be observed at the entrance of the pulmonary arteries.

In the case of the chronic implant, the flow structures are similar and thus are not shown here. The main difference resides in the magnitude of the vortex strengths and turbulence levels, consistent with the better pressure recovery measured in Section 3.3.

3.5. Mean Wall Shear Stress

Another important parameter when evaluating the performance of the pump is the shear stress at the blood vessel walls. Indeed it is necessary to ensure that the impeller will not damage the vessels, which could lead to rupture. Figure 18 shows the time averaged wall shear stresses for all three cases. Figure 18-a shows the wall shear stresses for the un-powered case. It can be seen that the stresses are low (below 5 Pa), with close to 0 values in regions of high re-circulation, mostly around the TCPC junction and in the VCs where the curvature of the vessels is large. Figure 18-b shows the wall shear stresses when the VIP is rotating at 3000 RPM inside the existing blood vessel configuration. It can be seen now that the peak is 15 Pa, at the vessel wall close to the tips of the VIP fins. This peak value is below typically accepted value, and is very localized. When the chronic implant is in place and rotating at 3000 RPM (Figure 18-c), the peak wall shear stress drops to 13 Pa, and is still localized near the rotating impeller. These results show a double advantage of the chronic implant over the temporary one. First, the maximum wall shear stresses are lower in the case of the chronic device, which is due to the fact that the minimum distance between the impeller and the wall is optimized and always constant. In the case of the temporary implant, the impeller had to be placed as well as possible inside the existing configuration, which may result in the impeller being very close to the blood vessel walls, thus increasing the local stresses. Second, the locations of the high wall shear stresses in the case of the chronic implant are where the housing is sitting, meaning that the wall stresses are not damaging any blood vessels.

3.6. Hemolysis Estimation

Hemolysis is another important parameter when evaluating the performance of a pump in blood flow. Indeed, too high damage would result in lower red blood cell concentration, as well as potential thrombosis and blood clotting. To estimate the hemolysis for all cases, we used the particle tracking method mentioned in Section 2.4.3. Particles were seeded at each inlet such that 10000 new particles would enter the domain during each cardiac cycle, and data were gathered over 15 cardiac cycles. The particles were assumed to have similar properties as red blood cells, with a diameter of $7\mu m$ and a density of 1150 $kg \cdot m^{-3}$. Once a particle crosses the outlet plane, the value of hemolysis index is saved and the statistics are then processed after the simulation. The particles are also used to estimate the hepatic factor distribution. The hepatic factor is a substance released in a blood stream by the liver, and is necessary to prevent the development of arteriovenous malformations in the lungs. It is then important that the flow coming from the IVC is split almost equatlly between the two lungs. For this particular blood vessel configuration, the offset between the two VCs is almost negligible, resulting in a good mixing of the two inlet streams at the junction of the TCPC, thus allowing a good split of the IVC flow between the two PAs. For the un-powered

simulation, the IVC flow split between LPA and RPA was close to 57% / 43%. When the temporary impeller is in place, because of the position of the VIP that maintains a good symmetry of the TCPC junction, the IVC flow split is maintained and statistical results showed a flow split of 58% / 42%. When the chronic implant is in place at the TCPC junction, the geometry of the junction is now fully controlled and symmetrical, resulting in an improvement of the hepatic factor distribution with a flow split of 52% / 48%.

Figure 19 shows the statistical data for the hemolysis index of the particles leaving the computational domain. This figure shows the probability of a particle to have a value of hemolysis index within a particular range when leaving the computational domain through one of the 26 outlets. Before surgery, it can be seen that most of the particles (60 %) have a value of less or equal to 5×10^{-5}, about 20 % have a value between 5×10^{-5} and 1.5×10^{-4} and the rest have a value above 1.5×10^{-4}. These remaining particles are particles that got trapped in boundary layer regions in which they were exposed to shear stresses for a longer time. When the chronic implant is present and rotating at 1000 RPM, it can be seen that once again the hemolysis is low. The main difference between this case and the case without the presence of the VIP is that the probability of finding particles with hemolysis index higher than 2.5×10^{-4} is higher. When the impeller is spinning at 3000 RPM, the probability to find particles with a value lower than 5×10^{-5} decreases (below 35 %) and the hemolysis index increases in average for all particles. It can be observed that the difference between the temporary and chronic implants is very small when looking at potential blood damage. Overall the values of hemolysis index are below accepted values for blood damage.

4. Conclusion

In this study, two solutions to improve the physiology of the Fontan circulation are presented. These two solutions are being developed in our research group and consist in implanting a rotating impeller inside the junction of the TCPC to increase the overall pressure recovery between vena cavae and pulmonary arteries. In the case of temporary implant, the impeller would be inserted via a catheter and would be used temporarily as a bridge-to-recovery or bridge-to-transplant. The second option consists of implanting a chronic housing containing the impeller in place of the existing TCPC junction. The housing would allow the pump to stay inside the patient indefinitely (even if it fails to rotate and reverts to serve as a static flow diverter), and allows for optimization of the performance of the pump by controlling the shape of the TCPC junction. To study the hemodynamics induced by this device, a Large Eddy Simulation solver was developed and coupled with a Multiblock Immersed Boundary Method to handle efficiently complex geometry on a simple Cartesian mesh. The solver is also coupled with particle tracking, allowing the user to simulate blood cells, thus estimating the hemolysis resulting from the mechanical support. Three cases were considered: the original patient specific geometry served as a baseline to estimate later the performance of the VIP. Then the temporary implant configuration was studied. The implantation of the chronic implant was performed via a Computational Surgery with the help of pediatric cardiac surgeons. Once the position of the chronic device was approved by the surgeons, evaluation of the performance was performed using the developed solver. Results showed very complex flows at different phases of the velocity inflow. Mean pressure rise showed that, at an identical RPM, the chronic implant performed

better, showing results similar to the ones obtained in an idealized TCPC [13], showing that the impact of the patient specific geometries can be limited by the presence of the housing. Mean wall shear stresses showed that the stresses were lower in the case of the chronic implant due to the optimized position of the VIP, which could not be achieved when using the existing blood vessel configuration. In all cases, the stresses were lower than generally accepted values for vessel damage. Finally, hemolysis estimation showed low values of hemolysis index for all cases, with similar values measured for the temporary and chronic implants.

Acknowledgments

The authors would like to acknowledge Pr. Alison Marsden for providing patient specific geometries and information related to flow boundary conditions. The authors would like to also acknowledge SimVascular (www.simvascular.org) that was used to create the patient specific geometry. The authors would also like to acknowledge financial support for this work by the National Institute of Health (NIH) (Grant no. HL098353) and Zeff Fellowship Trust.

References

1. Andersson M, Lantz J, Ebbers T, Karlsson M. Quantitative Assessment of Turbulence and Flow Eccentricity in an Aortic Coarctation: Impact of Virtual Interventions. Cardiovascular Engineering and Technology. 2015; 6:281–293. [PubMed: 26577361]
2. Armenio V, Fiorotto V. The importance of the forces acting on particles in turbulent flows. Physics of Fluids. 2001; 13:243–244.
3. Anupindi K, Delorme Y, Shetty D, Frankel S. A novel multiblock immersed boundary method for large eddy simulation of complex arterial hemodynamics. Journal of Computational Physics. 2013; 254:200–218.
4. Arvand A, Hahn N, Hormes M, Akdis M, Martin M, Reul H. Comparison of hydraulic and Hemolytic Properties of Different Impeller Designs of an Implantable Rotary Blood Pump by Computational Fluid Dynamics. Artifical Organs. 2004; 28:892–898.
5. Ashby S, Falgout R. A parallel multigrid preconditioned conjugate gradient algorithm for groundwater flow simulations. Nuclear Science and Engineering. 1996; 1:145–159.
6. Ashburn D, McCrindle B, Tchervenkov C, Jacobs M, Lo G, Bove E, Spray T, Williams W, Blackstone E. Outcomes after the Norwood operation in neonates with critical aortic stenosis or aortic valve atresia. The Journal of Thoracic and Cardiovascular Surgery. 2003; 125:1070–1082. [PubMed: 12771881]
7. Bazilevs Y, Calo V, Cottrell J, Hugues T, Reali A, Scovazzi G. Variational multiscale residual-based turbulence modeling for large eddy simulation of incompressible flows. Computer Methods in Applied Mechanics and Engineering. 2007; 197:173–201.
8. Botto L, Correa A, Erickson J. Racial and temporal variations in the prevalence of heart defects. Pediatrics. 2001; 107(3):E32. [PubMed: 11230613]
9. Bludszuweit C. Three dimensional numerical prediction of stress loading of blood particles in a centrifugal pump. Artificial Organs. 1995; 19:590–596. [PubMed: 8572957]
10. Dasi L, Pekkan K, Katajima H, Yoganathan A. Functional analysis of Fontan energy dissipation. Journal of Biomechanics. 2008; 41:2242–2252.
11. Davidson, L., Farhanieh, B. Thermo and Fluid Dynamics. Chalmers University of Technology; Gothenburg: 1992. CALC-BFC: A Finite-Volume Code Employing Collocated and Heat Transfer in Complex Three-Dimensional Geometries.
12. Deleval M. The Fontan circulation: What have we learned? What to expect? Pediatric Cardiology. 1998; 19:316–320. [PubMed: 9636255]
13. Delorme Y, Anupindi K, Kerlo AE, Shetty D, Rodefeld M, Chen J, Frankel S. Large eddy simulation of powered Fontan hemodynamics. Journal of Biomechanics. 2013; 46:408–422. [PubMed: 23177085]

14. Delorme Y, Anupindi K, Frankel S. Large eddy simulation of FDA's idealized medical device. Cardiovascular Engineering and Technology. 2013; 4:4.
15. Fontan F, Baudet E. Surgical repair of tricuspid atresia. Thorax. 1971; 26:240–248. [PubMed: 5089489]
16. Djomehri J, Biswas R. Performance Enhancement Strategies for Multi-Block Overset Grid CFD Applications. NAS Technical Report NAS-03-011. 2003
17. Fadlun E, Verzicco R, Orlandi P, Mohd-Yusof J. Combined immersed boundary finite difference methods for three dimensional complex flow simulations. Journal of Computational Physics. 2000; 161:35–60.
18. Falgout R, Jones J. Multigrid on massively parallel architectures. Lectures Nodes in Computational Science and Engineering. 2000
19. Falgout R, Yang. Hypre: a library of high performance preconditioners. Lectures Nodes in Computer Science. 2002; 2331:632–641.
20. Ge L, Dasi L, Sotiropoulos F, Yoganathan A. Characterization of Hemodynamic Forces Induced by Mechanical Heart Valves: Reynolds vs. Viscous Stresses. Annals of Biomedical Engineering. 2007; 36:276–297. [PubMed: 18049902]
21. Gillum R. Epidemiology of congenital heart disease in the United States. American Heart Journal. 1994; 127:919–927. [PubMed: 8154432]
22. Guha A. Transport and deposition of particles in Turbulent and Laminar flows. Annual reviews of Fluid Mechanics. 2008; 40:311–341.
23. Heuser G, Opitz R. A couette viscometer for short time shearing in blood. Biorheology. 1980; 17:17–24. [PubMed: 7407346]
24. Jeong J, Hussain F. On the identification of a vortex. Journal of Fluid Mechanics. 1994; 285:69–94.
25. Kerlo AE, Delorme Y, Xu D, Frankel S, Giridharan G, Rodefeld M, Chen J. Experimental characterization of powered Fontan hemodynamics in an idealized total cavopulmonary connection model. Experiments in Fluids. 2013; 54:1581.
26. Khunatorn Y, Shandas R, DeGroff C, Mahalingam S. Comparison of In Vitro Velocity Measurements in a Scaled Total Cavopulmonary Connection with Computational Predictions. Annals of Biomedical Engineering. 2003; 31:810–822. [PubMed: 12971614]
27. Makris E, Neofytou P, Tsangaris S, Housiadas C. A novel method for the generation of multi-block computational structures grids from medical imaging of arterial bifurcations. Medical Engineering and Physics. 2012; 34:1157–1166. [PubMed: 22209311]
28. Mark A, van Wachem B. Derivation and validation of a novel implicit second order accurate immersed boundary method. Journal of Computational Physics. 2008; 227:6660–6680.
29. Marsden A, Vignon-Clementel I, Chan F, Feinstein J, Taylor C. Effects of Exercise and Respiration on Hemodynamic Efficiency in CFD Simulations of the Total Cavopulmonary Connection. Annals of Biomedical Engineering. 2007; 35:250–263. [PubMed: 17171509]
30. Marsden A, Bernstein A, Reddy M, Shadden S, Spilker R, Chan F, Taylor C, Feinstein J. Evaluation of a novel Y-shaped extracardiac Fontan baffle using computational fluid dynamics. The Journal of Thoracic and Cardiovascular Surgery. 2009; 137:394–403. [PubMed: 19185159]
31. Marsden A, Moghadam M. Multiscale Modeling of Cardiovascular Flows for Clinical Decision Support. Applied Mechanics Reviews. 2015; 67(3):030804.
32. Marsden M, Feinstein J. Computational modeling and engineering in pediatric and congenital heart disease. Current opinion in pediatrics. 2015; 27(5):587–596. [PubMed: 26262579]
33. Migliavacca F, Dubini G, Bove E, deLeval M. Computational fluid dynamics simulations in realistic 3D geometries of the total cavopulmonary anastomosis: the influence of the inferior caval anastomosis. Journal of Biomechanical Engineering. 2003; 805:805–813.
34. Hsia T, Migliavacca F, Pittaccio S, Radaelli A, Dubini G, Pennati G, de Leval M. Computational Fluid Dynamic Study of Flow Optimization in Realistic Models of the Total Cavopulmonary Connections. Journal of Surgical Research. 2004; 116:305–313. [PubMed: 15013370]
35. Mittal R, Simmons S, Udaykumar H. Application of Large Eddy Simulation to the Study of Pulsatile Flow in a Modeled Arterial Stenosis. Journal of Biomechanical Engineering. 2001; 123:325–332. [PubMed: 11563757]

36. Nilsson, H., Davidson, L. Thermo and Fluid Dynamics. Chalmers University of Technology; Gothenburg: 1998. CALC-PVM: A parallel SIMPLEC multiblock solver for turbulent flow in complex domains.
37. Nilsson, H. Thermo and Fluid Dynamics. Chalmers University of Technology; Gothenburg: 1999. A Numerical Investigation of the Turbulent Flow in a Kaplan Water Turbine Runner.
38. Nilsson H, Dahlstrom S, Davidson L. Parallel multiblock CFD computations applied to industrial cases. Parallel Computational Fluid Dynamics-Trends and Applications. 2001
39. Ohye R, Sleeper L, Mahony L, Newburger J, Pearson G, Lu M, Goldberg C, Tabbutt S, Frommelt P, Ghanayem N. Comparisons of shunt types in the norwood procedure for single ventricle lesions. New England Journal of Medicine. 2010; 362:1980–1992. [PubMed: 20505177]
40. http://www.vascularmodel.com/sandbox/doku.php?id=start
41. Pope, S. Turbulent flows. Cambridge University Press; 2000.
42. Plunkett M, St Louis J. Mechanical Circulatory Support Devices in Pediatric Patients. Handbook of Cardiac Anatomy, Physiology, and Devices. 2015:187–197.
43. Pundi K, Johnson J, Dearani J, Li Z, Hinck C, Dahl S, Cannon B, O'Leary P, Driscoll D, Cetta F. 40-year Follow Up After the Fontan Operation: Long Term Outcomes of 1052 Patients. Journal of the American College of Cardiology. 2015; 66:1700–1710. [PubMed: 26449141]
44. Rodefeld M, Boyd J, Myers C, Lalone B, Bezruczko A, Potter A, Brown J. Cavopulmonary assist: Circulatory Support for the Univentricular Fontan Circulation. Annals of Thoracic Surgery. 2003; 76:1911–1916. [PubMed: 14667610]
45. Rodefeld M, Coats B, Fisher T, Giridharan G, Chen J, Brown J, Frankel S. Cavopulmonary assist for the univentricular Fontan circulation: Von Karman Viscous Impeller Pump. The Journal of Thoracic and Cardiovascular Surgery. 140:529–536.
46. Ryu K, Healy M, Ensley A, Sharma S, Lucas S, Yoganathan A. Importance of Accurate Geometry in the Study of the Total Cavopulmonary Connection: Computational Simulations and In Vitro Experiments. Annals of Biomedical Engineering. 2001; 29:844–853. [PubMed: 11764315]
47. Situ, Y., Liu, L., Martha, C., Louis, M., Li, Z., Sameh, A., Blaisdell, G., Lyrintzis, A. A Communication-efficient Linear System Solver for Large Eddy Simulation of Jet Engine Noise. Cluster Computing (special edition with selected papers from the IEEE International Conference on Cluseter Computing); 2011.
48. Song X, Throckmorton A, Wood H, Antaki J, Olsen D. Computational Fluid Dynamics Prediction of Blood Damage in a Centrifugal Pump. Artificial Organs. 2003; 27:938–941. [PubMed: 14616540]
49. Shetty D, Fisher T, Chunekar A, Frankel S. High order incompressible large eddy simulation of fully inhomogeneous turbulent flows. Journal of Computational Physics. 2010; 229:8802–8822.
50. Shetty D, Jie S, Chandy A, Frankel S. A pressure correction scheme for rotational navier stokes equations and its application to rotating turbulent flows. Communications in Computational Physics. 2011; 9:740–755.
51. Soerensen D, Pekkan K, de Zelicourt D, Sharma S, Kanter K, Fogel M, Yoganathan A. Introduction of a New Optimized Total Cavopulmonary Connection. The Annals of Thoracic Surgery. 2007; 83:2182–2190. [PubMed: 17532420]
52. Sotiropoulos F, Borazjani I. A review of state of the art numerical methods for simulating flow through mechanical heart valves. Medical and Biological Engineering and Computing. 2009; 47:243–256.
53. Taskin M, Fraser K, Zhang T, Gellman B, Fleishi A, Dasse K, Griffith B, Wu Z. Computational Characterization of Flow and Hemolytic Performance of the UltraMag Blood Pump for Circulatory Support. Artificial Organs. 2010; 34:1099–1113. [PubMed: 20626739]
54. Teigland R, Eliassen I. A multiblock / multilevel mesh refinement procedure for CFD computations. International Journal for Numerical Methods in Fluids. 2001; 36:519–538.
55. Throckmorton A, Ballman K, Myers C, Litwak K, Frankel S, Rodefeld M. Mechanical Cavopulmonary Assist for the Univentricular Fontan Circulation Using a Novel Folding Propeller Blood Pump. American Society of Artificial Internal Organs. 53:734–741.
56. Varghese S, Frankel S, Fisher P. Direct numerical simulation of stenotic flows. Part 1. Steady flow. Journal of Fluid Mechanics. 2007; 582:253–280.

57. Varghese S, Frankel S, Fisher P. Direct numerical simulation of stenotic flows. Part 2. Pulsatile flow. Journal of Fluid Mechanics. 2007; 582:281–318.

58. Xenos M, Girdhar G, Alemu Y, Jesty J, Slepian M, Einav S, Bluestein D. Device Thrombogenicity Emulator (DTE) - Design optimization methology for cardiovascular devices: A study in two bileaflet MHV designs. Journal of Biomechanics. 2010; 43:2400–2409. [PubMed: 20483411]

59. Zhang J, Jackson T. A high order incompressible flow solver with WENO. Journal of Computational Physics. 2009; 228:2426–2442.

Highlights

- First computational surgical implantation of a novel pump for Fontan circulation
- Multiblock approach improves accuracy / efficiency of IBM for internal flows
- IBM on fixed Cartesian grid allows simulations of flows in complex moving geometry
- LES model allows accurate prediction of pathological low Re transitional flows
- Pump provides desired pressure rise while keeping blood damage low

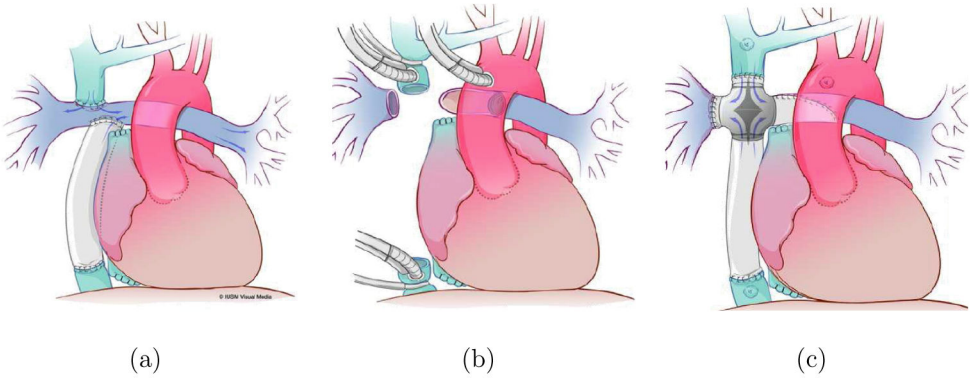

Figure 1.
Three steps of the procedure. (a) Extracardiac conduit Fontan. (b) Cardiopulmonary bypass. (c) Pump implantation

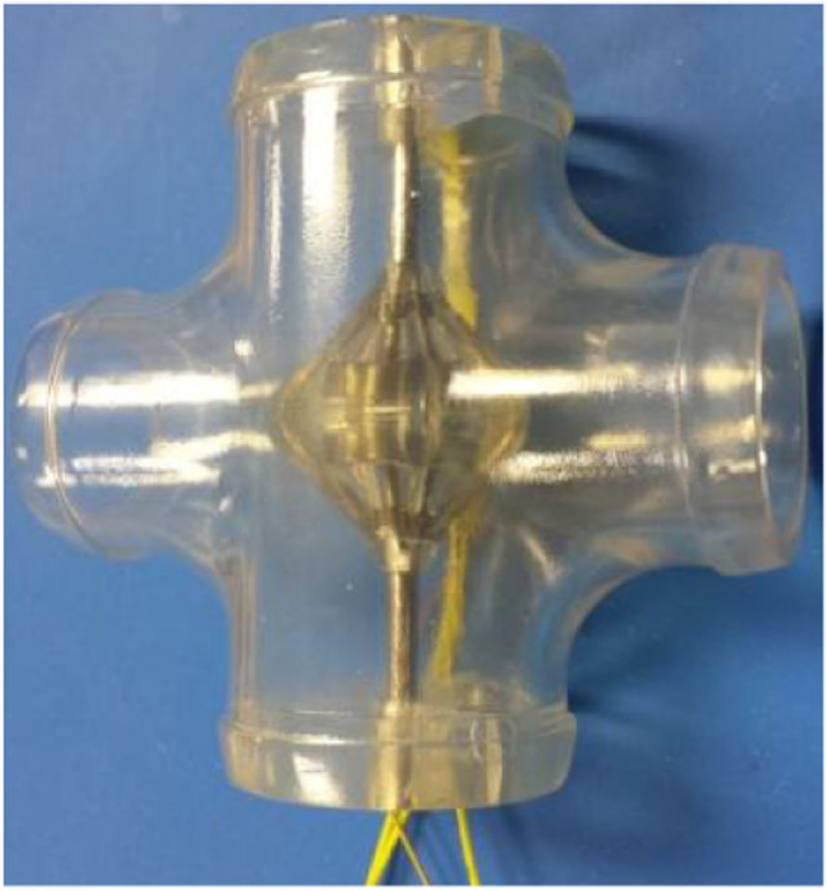

Figure 2.
Prototype under development. The transparent housing can be seen, as well as the VIP with the motor inside.

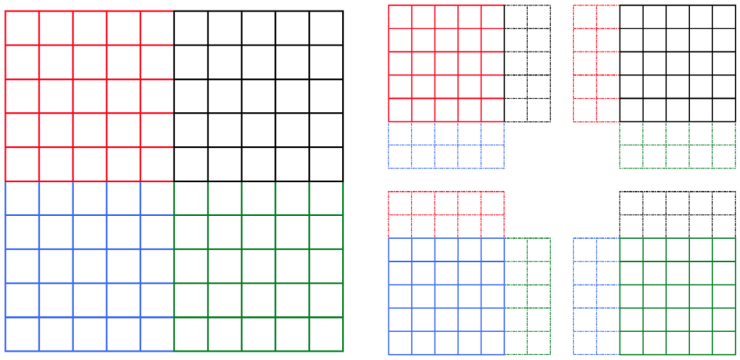

(a) 4 domains decomposition. (b) Overlapping of the 4 domains.

Figure 3.
Schematic of the domain decomposition.

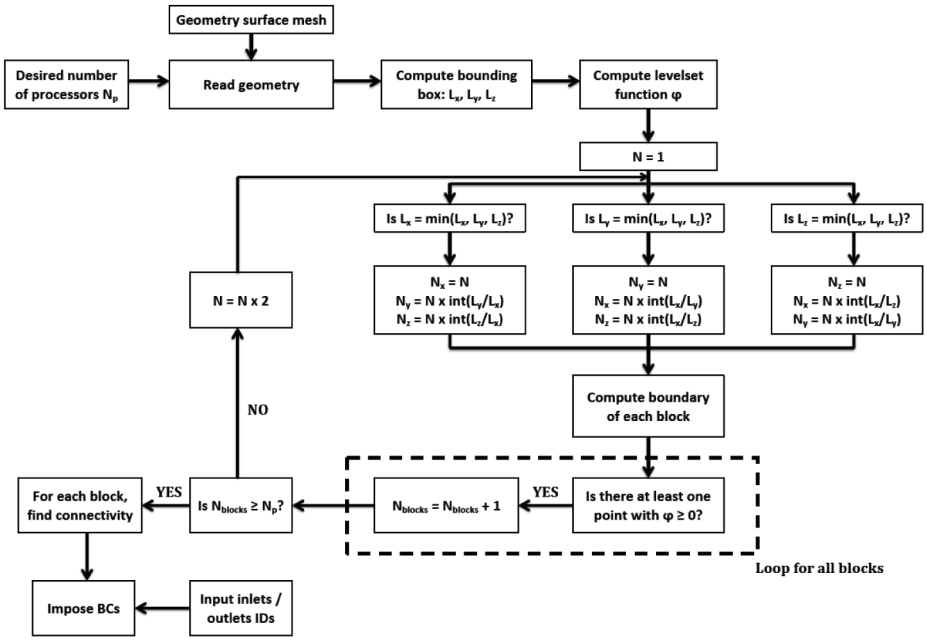

Figure 4.
Schematic of the iterative process to automatically setup the domain decomposition.

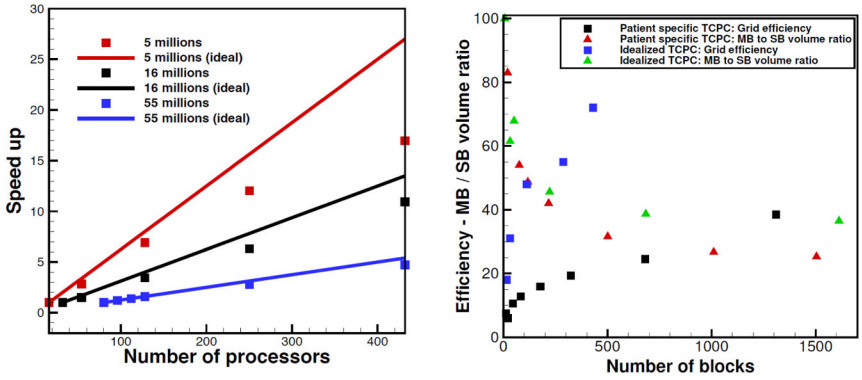

(a) Scaling of the solver.

(b) Efficiency of the multiblock decomposition.

Figure 5.
Overall computational efficiency of the solver.

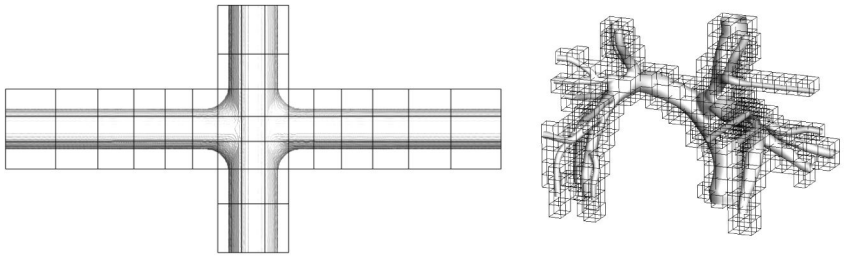

(a) Idealized geometry with 57 blocks. (b) Patient specific geometry with 546 blocks.

Figure 6.
Examples of domain decomposition for an idealized and a patient specific geometry.

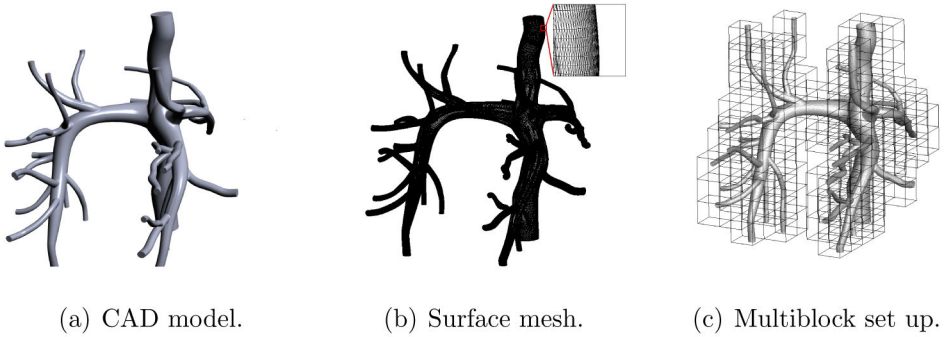

(a) CAD model. (b) Surface mesh. (c) Multiblock set up.

Figure 7.

Three steps of the overall set up of a simulation. First we start with a CAD model that is obtained from MRI deta (a). Then a surface mesh is generated (b) and is used to set up the overall computational domain (c).

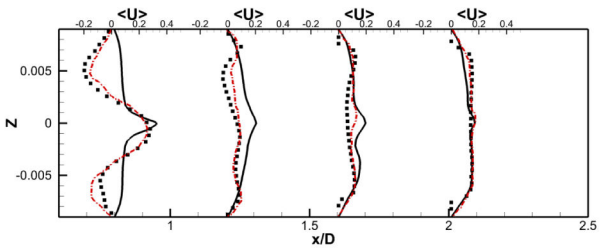

(a) u velocity.

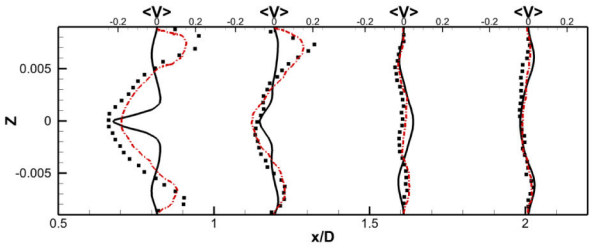

(b) v velocity.

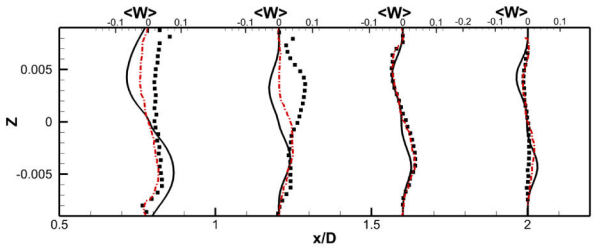

(c) w velocity.

Figure 8.

Comparisons of the predicted velocity components in the outlet pipe of the TCPC with experimental measurements. Black lines show the results obtained with the single block configuration ([13]), red dashed lines show the results obtained with the current multiblock approach, dots show the experimental measurements.

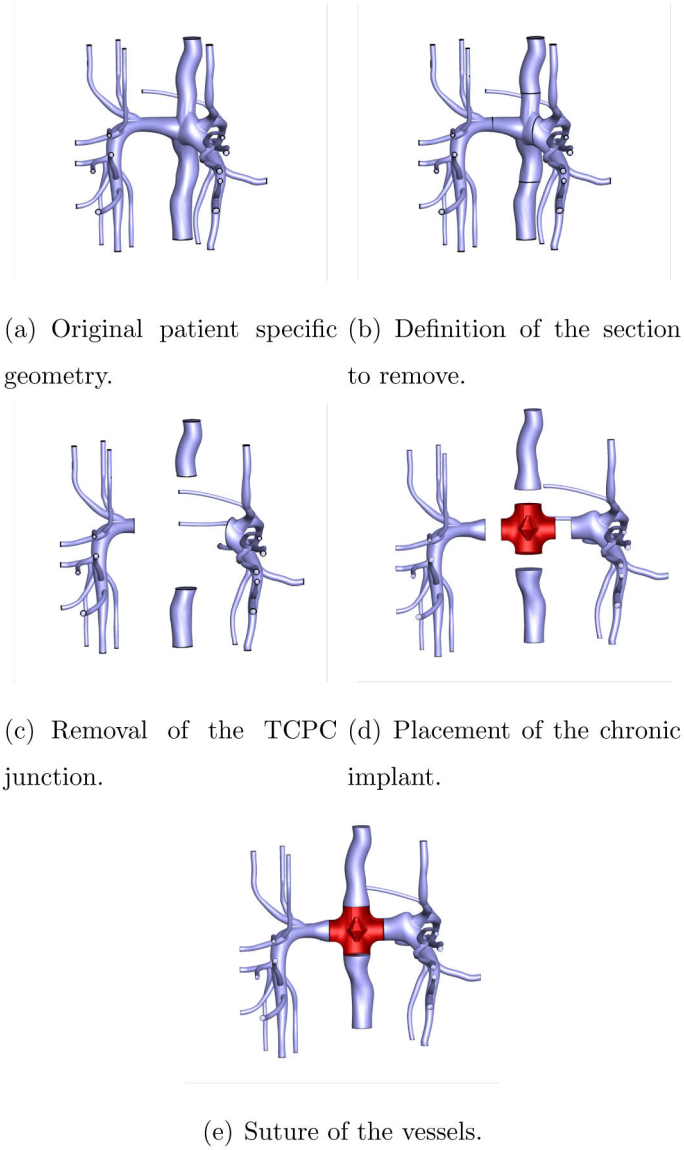

(a) Original patient specific geometry.

(b) Definition of the section to remove.

(c) Removal of the TCPC junction.

(d) Placement of the chronic implant.

(e) Suture of the vessels.

Figure 9.

Computational surgery to virtually implant the chronic device inside an existing patient specific configuration. From the original blood vessels (a), the section to be removed was defined (b) and the TCPC junction was cut (c). The chronic implant is then put in place and the vessels' ends are modified to match the size of the implant (d). Finally the blood vessels are sutured back to the implant.

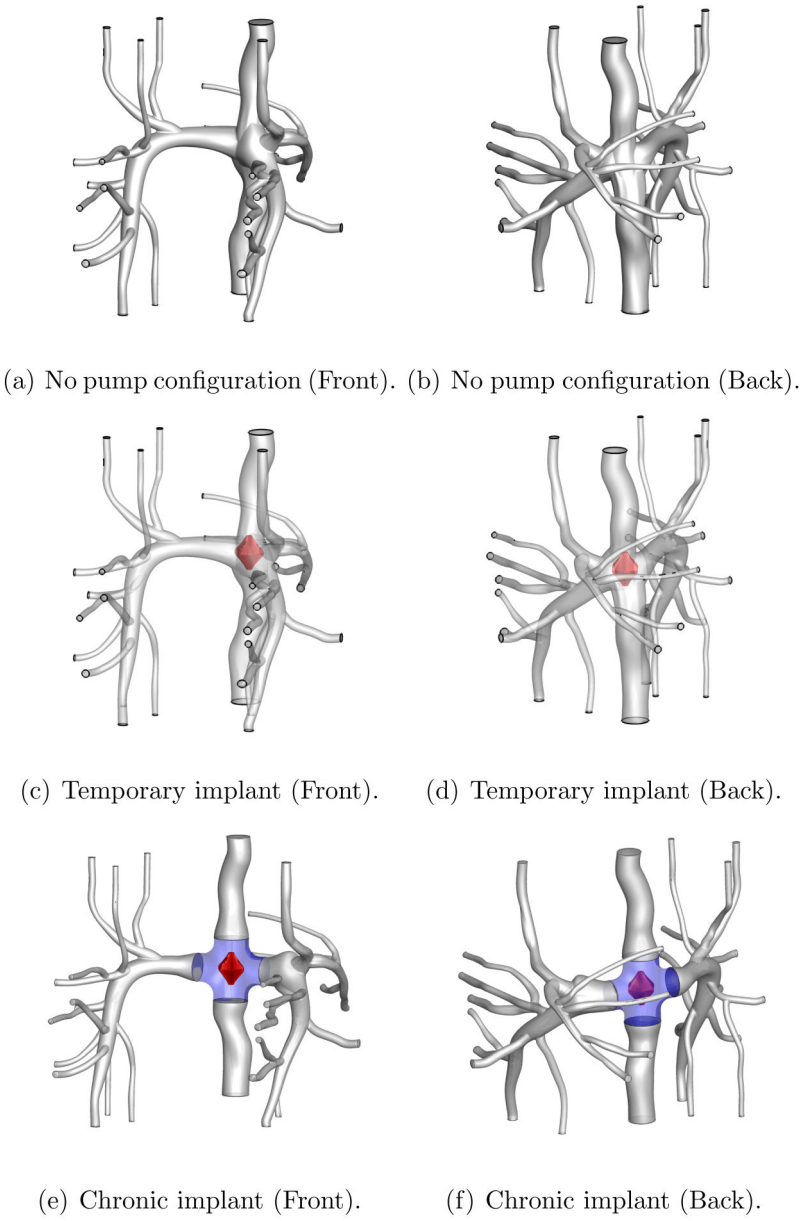

(a) No pump configuration (Front). (b) No pump configuration (Back).

(c) Temporary implant (Front). (d) Temporary implant (Back).

(e) Chronic implant (Front). (f) Chronic implant (Back).

Figure 10.

Three cases studies here. The original patient specific configuration is used as a baseline case to study the effect of the implant on the Fontan circulation ((a) and (b)). The effect of the temporary implant is studied to compare the performance with the chronic device ((c) and (d)). Finally the improvements of the performance due to the housing of the chronic implant are studied ((e) and (f)).

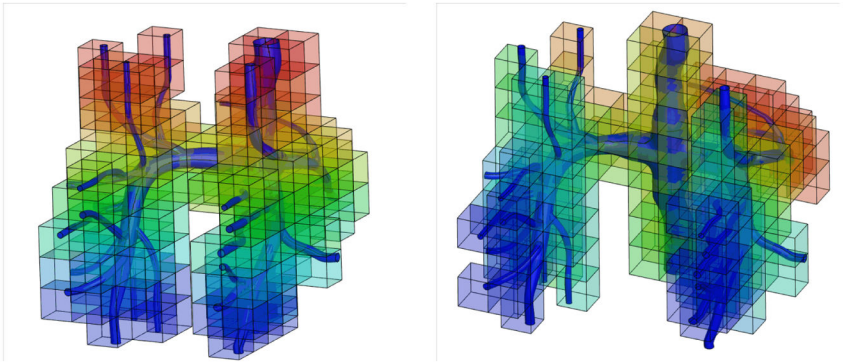

(a) No pump and temporary implant configurations.

(b) Chronic implant configuration.

Figure 11.

Domain decomposition for all simulations presented in this study. Each block is colored differently to facilitate the visualization of the computational domain.

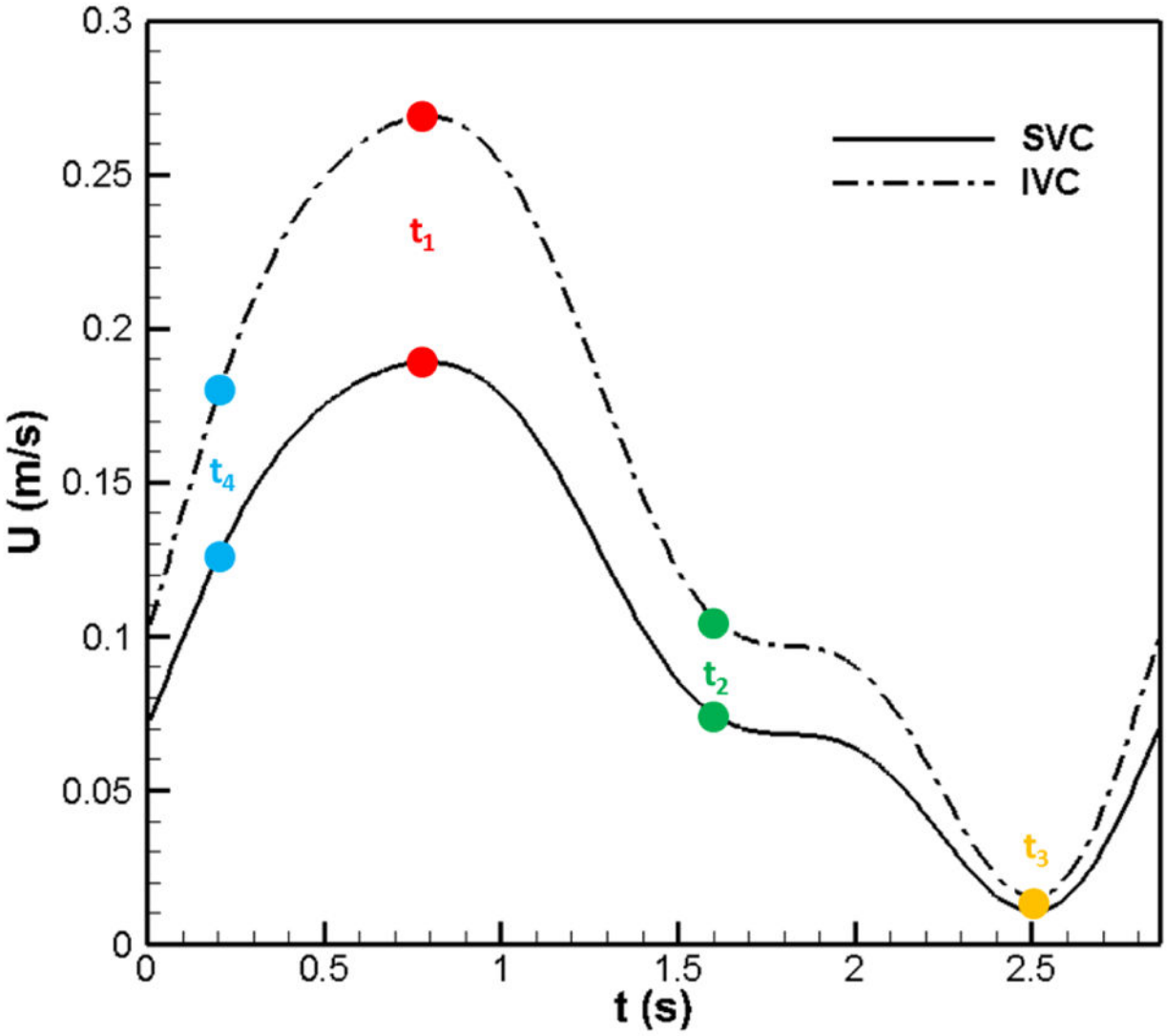

Figure 12.
Inflow velocity profiles at the IVC and SVC. The time points highlight the locations used in Section 3.4 to characterize the flow.

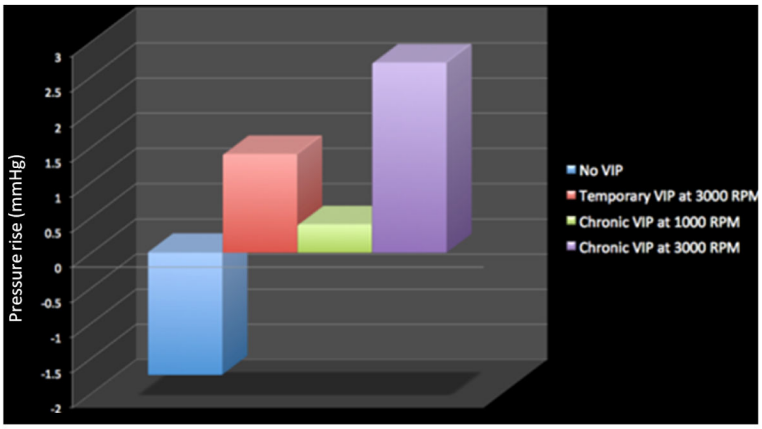

Figure 13.
Pressure rise between the VCs and the PAs

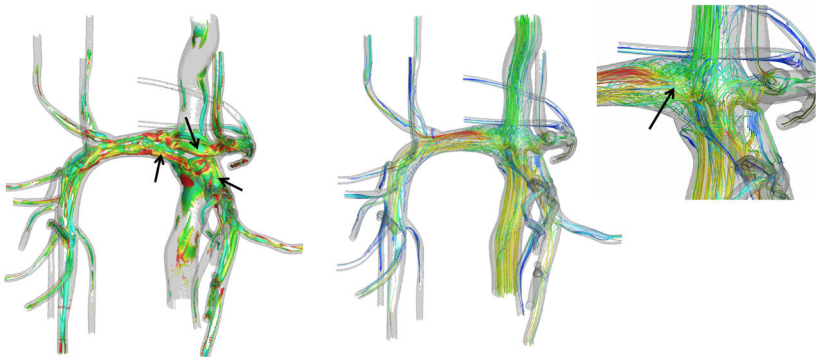

(a) t_1: λ_2 criterion colored by vorticity magnitude.

(b) t_1: Streamtraces colored by velocity magnitude.

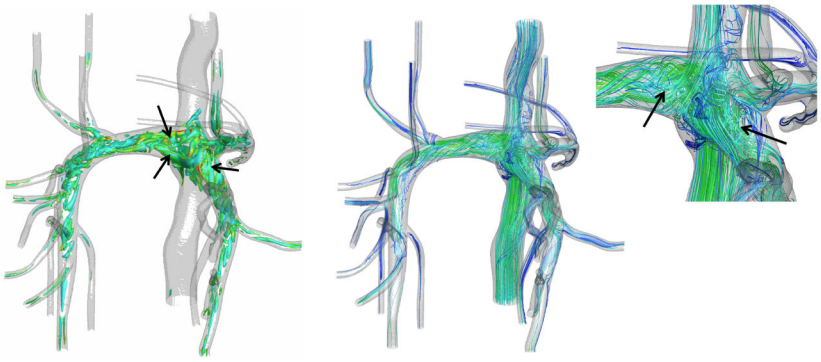

(c) t_2: λ_2 criterion colored by vorticity magnitude.

(d) t_2: Streamtraces colored by velocity magnitude.

Figure 14.
Instantaneous flow features: Unpowered case (1/2).

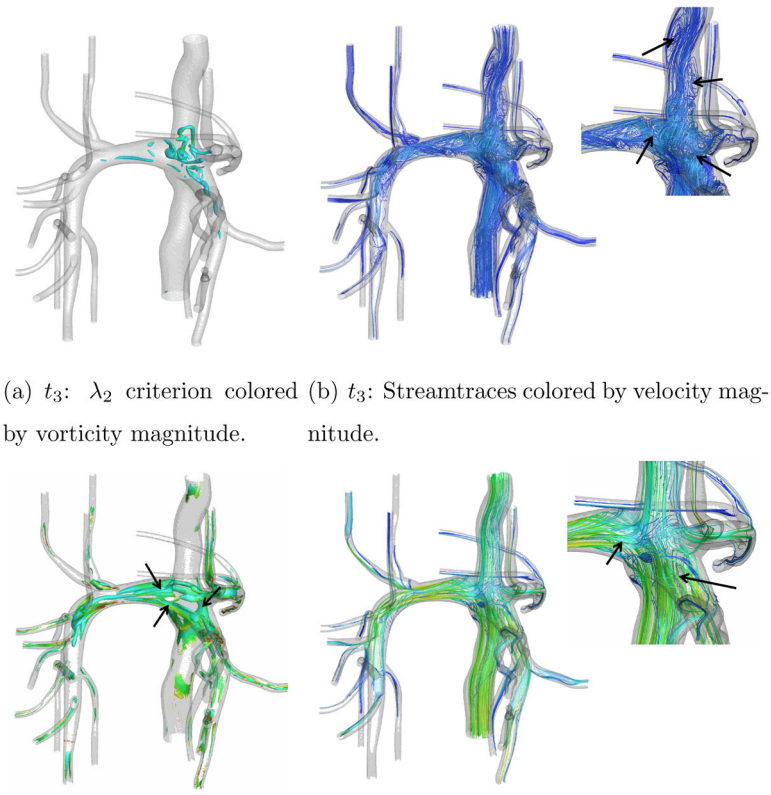

(a) t_3: λ_2 criterion colored by vorticity magnitude.

(b) t_3: Streamtraces colored by velocity magnitude.

(c) t_4: λ_2 criterion colored by vorticity magnitude.

(d) t_4: Streamtraces colored by velocity magnitude.

Figure 15.
Instantaneous flow features: Unpowered case (2/2).

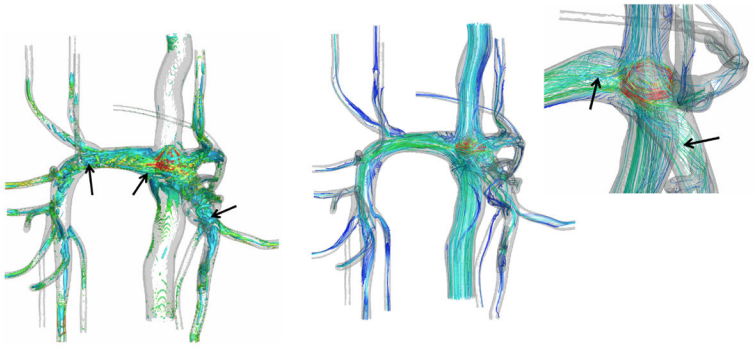

(a) t_1: λ_2 criterion colored by vorticity magnitude.

(b) t_1: Streamtraces colored by velocity magnitude.

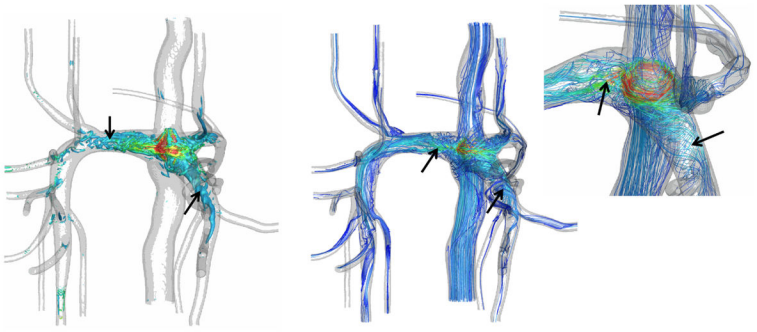

(c) t_2: λ_2 criterion colored by vorticity magnitude.

(d) t_2: Streamtraces colored by velocity magnitude.

Figure 16.
Instantaneous flow features: Temporary implant case at 3000 RPM(1/2).

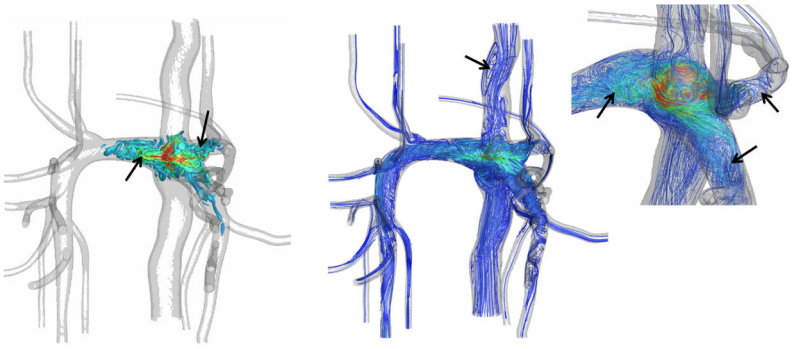

(a) t_3: λ_2 criterion colored by vorticity magnitude.

(b) t_3: Streamtraces colored by velocity magnitude.

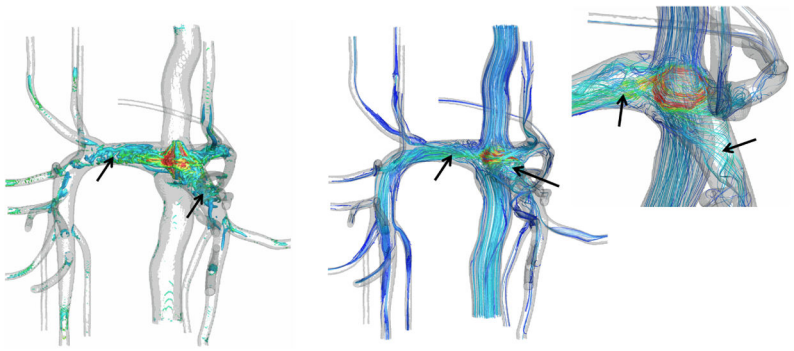

(c) t_4: λ_2 criterion colored by vorticity magnitude.

(d) t_4: Streamtraces colored by velocity magnitude.

Figure 17.
Instantaneous flow features: Temporary implant case at 3000 RPM (2/2).

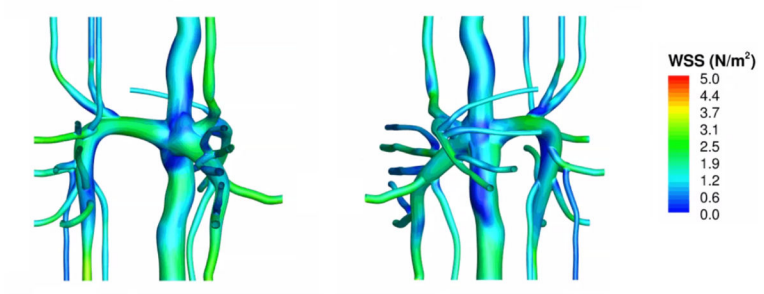

(a) No pump configuration.

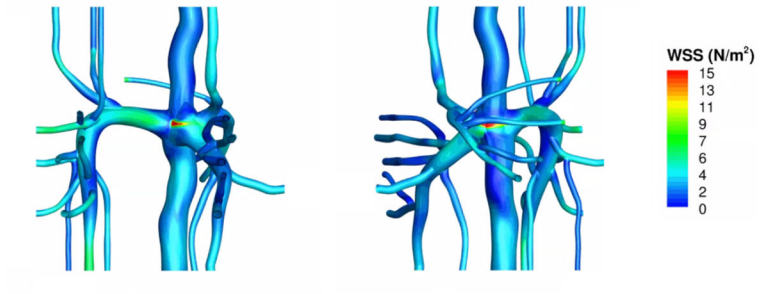

(b) Temporary implant configuration (3000 RPM).

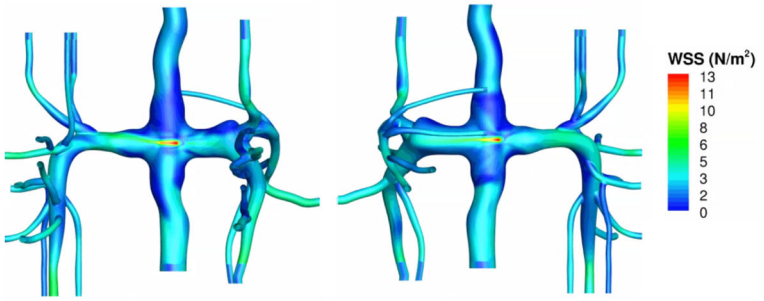

(c) Chronic Implant Configuration (3000 RPM).

Figure 18.
Mean wall shear stress.

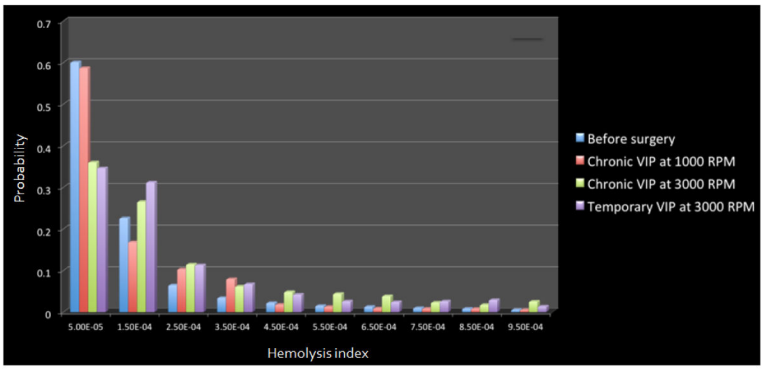

Figure 19.
Probability distribution of hemolysis index.